

Wide-field optical model of the human eye with asymmetrically tilted and decentered lens that reproduces measured ocular aberrations

JAMES POLANS,^{1,*} BART JAEKEN,² RYAN P. McNABB,^{3,1} PABLO ARTAL,² AND JOSEPH A. IZATT^{1,3}

¹Department of Biomedical Engineering and Fitzpatrick Institute of Photonics, Duke University, Durham, North Carolina 27708, USA

²Laboratorio de Óptica, Universidad de Murcia, Campus de Espinardo (Edificio 34), 30100 Murcia, Spain

³Department of Ophthalmology, Duke University Medical Center, Durham, North Carolina 27710, USA

*Corresponding author: james.polans@duke.edu

Received 23 June 2014; revised 2 December 2014; accepted 12 December 2014 (Doc. ID 214383); published 30 January 2015

Eye models are valuable tools that can help delineate the role of anatomical parameters on visual performance and guide the design of advanced ophthalmic instrumentation. We propose an optically accurate wide-field schematic eye that reproduces the complete aberration profile of the human eye across a wide visual field. The optical performance of the schematic eye is based on experimentally measured wavefront aberrations taken with a four mm pupil for the central 80° of the horizontal meridian (101 eyes) and 50° of the vertical meridian (10 eyes). Across the entire field of view, our model shows excellent agreement with the measured data both comprehensively and for low-order and high-order aberrations. In comparison to previous eye models, our schematic eye excels at reproducing the aberrations of the retinal periphery. Also unlike previous models, tilt and decentering of the gradient refractive index crystalline lens, which arose naturally through the optimization process, permits our model to mimic the asymmetries of real human eyes while remaining both anatomically and optically correct. Finally, we outline a robust reverse building eye modeling technique that is capable of predicting trends beyond those defined explicitly in the optimization routine. Our proposed model may aid in the design of wide-field imaging instrumentation, including optical coherence tomography, scanning laser ophthalmoscopy, fluorescence imaging, and fundus photography, and it has the potential to provide further insights in the study and understanding of the peripheral optics of the human eye. © 2015 Optical Society of America

OCIS codes: (330.4060) Vision modeling; (330.7326) Visual optics, modeling; (330.4460) Ophthalmic optics and devices; (330.7327) Visual optics, ophthalmic instrumentation; (170.4470) Ophthalmology; (170.4500) Optical coherence tomography.

<http://dx.doi.org/10.1364/OPTICA.2.000124>

1. INTRODUCTION

The human eye is an intriguing optical instrument whose behavior has been the focus of many investigations over the past century and a half. The human eye can be viewed optically as a multiple-element refractive imaging system composed of the cornea, pupil, lens, and retina. The unique features of the eye often behave like a nearly aplanatic system [1], where the shape and gradient refractive index (GRIN) distribution of the lens may help to reduce the spherical and coma aberrations

originating in the cornea. These optical characteristics permit analogs to be drawn to complex wide-field imaging lenses. Modeling the subtle intricacies of the optical properties of the human eye is important in order to better understand their roles in visual perception [2].

Optical models are valuable tools for understanding the performance of the many refracting surfaces of the eye. These models are used in many ophthalmic applications, including optometry, refractive surgeries such as photorefractive

keratectomy [3], laser-assisted *in situ* keratomileusis [4], and intraocular lens implantation [5,6]. Schematic eyes not only provide insight into the optical characteristics of the eye, but they also assist in didactic endeavors to identify, diagnose, and classify trends related to age [7–12], gender [13], ethnicity, and accommodation [14–18]. Model eyes can be helpful in understanding how anatomical changes affect the progression of certain pathologies such as myopia [19–21] as well.

Model eyes also have been incorporated into the design of imaging instruments [22,23] in order to predict the theoretical spot size of a beam on the retina, magnification, modulation transfer function, angular field of view, optical throughput, and the longitudinal chromatic aberration (LCA). The spot size ultimately dictates the imaging resolution of a system, which makes it a key feature in the design of many instruments. For specialized ophthalmic instrumentation aimed at imaging the periphery of the retina, the exactness of the model used in the simulation becomes increasingly important, as the magnitudes of the aberrations vary with eccentricity [19,24–28]. Therefore, it is surprising to find that an optically accurate wide-field schematic eye that aims to aid the design of modern imaging systems has not been created. Having a robust model eye that potentially could be utilized during a system's design to preemptively correct the aberrations inherent to the peripheral optics could enable high-resolution imaging modalities, including optical coherence tomography [29,30], scanning laser ophthalmoscopy [22], and fluorescence imaging [31,32], to extend their field of view to the peripheral retina. The peripheral retina presents a multitude of ocular pathologies including diabetic retinopathy [33], retinal vein occlusions [34], choroidal masses [35], vasculitis, uveitis, choroidal dystrophies, retinal tears and detachments, Coats' disease, familial exudative vitreoretinopathy, and incontinentia pigmenti.

Eye models date back as far as the mid 19th century, when Moser (1844) and Listing (1851) built schematic eyes using spherical surfaces as the cornea and lens [36]. These models were further improved by the work of Helmholtz and Tscherning until the widely accepted Gullstrand model [37] was introduced in 1909. The Gullstrand model physically resembled real eyes and utilized a shell structure as the crystalline lens, but due to the difficulty in tracing refracted light through a shell structure, the model was later simplified by Le Grand [38] and Emsley [39]. Modern eye modeling began taking form in the late 20th century with the advancement of the tools used to measure the optical quality of the eye. Lotmar [40] improved the eye models by adding aspheric surfaces in 1971, while the work of Kooijman [41] and Pomerantzeff [42] investigated the effects of a curved retina. Blaker adopted an adaptive model of the human eye in 1980 [43] and continued his work with an age- and accommodation-dependent model in 1991 [9]. Thibos *et al.* modeled the axial chromatic aberrations [44] and on-axis spherical aberration [45]. Next, Liou and Brennan [46] presented an anatomically inspired finite eye that used a GRIN lens. Escudero-Sanz and Navarro [47] developed a wide-field schematic eye by adding a curved imaging surface to an accommodation-dependent model [14]. Archison [8] contributed a tilted and decentered lens and retina, but he observed that the asymmetric model had

limited success in modeling the eye's peripheral refraction. Personalized eyes tailored to specific groups emerged soon thereafter, with models defined by Navarro *et al.* [48], Tabernero *et al.* [5], and Rosales and Marcos [49]. Later, Goncharov and Dainty incorporated a GRIN lens into their wide-field schematic eyes [50], creating separate models for each of three distinct age groups.

Each of the aforementioned eye models was designed with a unique goal in mind. The principal aim of some of the models was to simulate the correct magnitude of on-axis spherical aberration [45,51], while other models prioritized anatomical accuracy [40,46]. Age-dependent [8,50,52] and accommodation-dependent [8,14,16] eye models were another area of focus, as well as models that exhibited the correct quantity of chromatic aberrations [44,45]. The more recent models sought to better imitate the gradient index profile of the crystalline lens [52–54], especially in diseased eyes [55]. The existing eye models spanned a wide variety of applications, but no model has been able to portray accurately the full aberration profile across a wide field of view, including the naturally occurring asymmetries of the human eye.

Many of the previous model eyes were challenged by a lack of available aberration data at the time of conception. A detailed compilation of the experimentally measured data used in modern eye modeling was outlined succinctly in [8] and [50]. The large data sets that formed the basis of many fundamental properties of the eye included corneal topography, but they lacked a direct measurement of the optical aberrations. Instead, aberration profiles were derived from the anatomical geometry of the eye. Direct measurement of the aberration profiles was performed initially with laser ray-tracing and double-pass techniques [25,56,57], but the measurements were sparse and often originated from a sample population consisting of as few as four subjects. Due to the limited availability of aberration data, even some of the more recent models only made comparisons to existing eye models and not to experimental measurements. Evaluating a new eye model by how closely it resembled a previous model made it difficult to assess the validity of the new model as compared to human eyes. Furthermore, in multiple cases, the discussed performance metrics were based predominantly around on-axis spherical aberration rather than a full wide-field aberration profile.

Over the past few decades, considerable effort has been made to better understand ocular performance across the human visual field [19,24–28,47,50,58–65]. This effort has led to numerous technological advancements, including the adaptation of Shack–Hartmann wavefront sensors for ocular aberrometry [66–68] and the subsequent invention of special machinery capable of measuring the wavefront aberrations across a large field of view [65,69]. These tools contributed to a rich growth in the availability of peripheral wavefront aberration data [28].

In an effort to supplement the existing eye models with the latest wavefront data, one of our goals was to compare the optical performance of eye models directly with experimentally measured aberration profiles [70]. Additionally, we combined the recently acquired aberration data into our own eye model

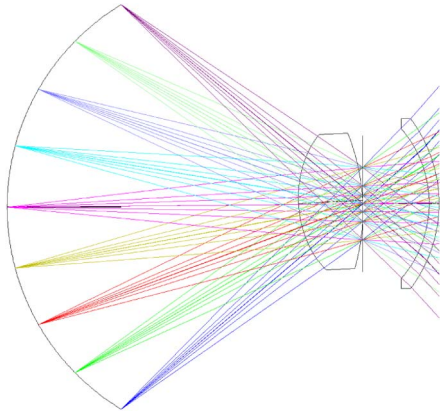


Fig. 1. Schematic ray trace of the proposed model eye. The colored lines represent point sources that originated from various retinal eccentricities spanning a $\pm 40^\circ$ angle range in the pupil.

humor based on Archison and Smith's findings [73]. The chromatic response of the GRIN lens (Table 3) was implemented using the information provided in [74], which examined specifically the chromatic aberrations across a wide field of view for human eyes. Following the work of [16], we used a biconic anterior and posterior corneal surface. Additionally, we permitted the crystalline lens to be displaced transversally to the optical axis and to be rotated in any plane.

In contrast to the previous eye models, which were developed for 6–8 mm pupil diameters, our eye model was designed around a pragmatic pupil size of 4 mm in order to pair our model eye with wavefront data acquired under normal viewing conditions. Additionally, the model was optimized with light that originated at a point source on the retina and propagated to the cornea, because this orientation most accurately mimicked the Shack–Hartmann wavefront sensor measurements.

With the optical dispersion and initial surface topologies set, a custom merit function was written for the optimization process (see Supplement 1). Anatomical boundary limits were imposed using values previously reported in the literature [16,75]. Since the anterior and posterior surface curvatures, conical constants, and GRIN of the crystalline lens cannot be measured readily *in vivo*, the lens' boundary conditions were given less weight than those parameters that had been validated consistently, such as corneal biometry. The works of [48,76,77] have previously demonstrated merit functions that constrain successfully the anatomical features of an eye model.

Additionally, we constrained the ocular aberrations as a function of retinal eccentricity. Our model's aberrations were set to match the average values that were measured in the right eye along the horizontal (101 eyes) and vertical (10 eyes) meridians. Please note that the data presented throughout this work represented those aberrations pertaining to the right eye. A similar optimization process can be performed in order to obtain a left eye model, but the differences between the right and left eyes were not essential within the context of this work. The first 15 Zernike terms (through fourth order) using the Optical Society of America standard notation were entered into the merit function from retinal eccentricities ranging from -40° to $+40^\circ$ in 10° steps along the horizontal meridian and -20° to $+20^\circ$ in 10° steps along the vertical meridian. Piston, tip, and tilt were not included in the merit function because they could represent artifacts of the aberration measurement system. Because we desired an optically accurate wide-field eye model, we gave the aberrations of all eccentricities significant weight during the optimization process, but favored the aberrations closer to the visual axis by assigning them greater weight (10 \times) than those pertaining to the periphery. An example optimization merit function is provided in Table S1 of Supplement 1.

Prior works have reported a crystalline lens decentration of ~ 0.20 mm [8,78] and tilt [79–82] of $\sim 4^\circ$, but the standard deviations of these measurements were of the same order as the magnitude, so we permitted these parameters to vary without restriction. Similar magnitudes and variations for decentration and tilt have been validated by Purkinje-based imaging systems as well [83,84].

3. RESULTS

After optimization, the resulting eye model was used to generate a plethora of data in Zemax. The optical power of our eye model was found to be 62.3 D on-axis for a paraxial beam. The lens power was 20.4 D, which was in agreement with studies based on magnetic resonance imaging [85] and on refraction correction [8]. The entrance pupil was located 3.64 mm posterior to the apex of the lens, while the exit pupil was located 3.54 mm in front of the lens. The longitudinal spherical aberration was calculated as the difference in axial distance between the focal points of the marginal and paraxial rays; it was determined as 0.290 mm for a pupil diameter of 4 mm. Using a 6 mm pupil diameter at 633 nm, our model predicted

Table 2. Schott Dispersion Coefficients of Eye Model Media

Surface	a_0	a_1	a_2	a_3	a_4	a_5
Vitreous Humor	1.7494E + 00	-5.2758E - 04	1.4299E - 02	-1.4114E - 03	1.1750E - 04	8.6476E - 07
Aqueous Humor	1.7471E + 00	-2.5796E - 04	1.5845E - 02	-1.7850E - 03	1.5126E - 04	7.3259E - 07
Cornea	1.8535E + 00	2.8269E - 04	1.6610E - 02	-1.8719E - 03	1.6283E - 04	1.5807E - 07

Table 3. Sellmeier Dispersion Coefficients of Crystalline Lens ($n_{\text{ref}} = 555\text{nm}$)

K_{11}	K_{12}	K_{21}	K_{22}	K_{31}	K_{32}	L_1	L_2	L_3
-543.4493	784.8531	269.8803	-389.7629	273.6147	-395.1561	-0.0010	0.0000	-0.0020

0.106 μm of spherical aberration as compared to the mean values of 0.120 [86] and 0.138 μm [87] reported previously for 6 mm pupils. The total length of our model eye was 23.77 mm, which was within the range reported by [79]. Even though these optical properties were not constrained explicitly in the merit function, they assumed values consistent with prior literature. Table 1 lists the structural parameters of the various components of the eye model, all of which fell within the anatomically constrained boundaries of measured data.

Figure 1 shows a 2D ray trace of the sagittal cut of our eye model. The colored lines represent those rays that originated from a common point source on the retina. The chief ray of each set of rays formed an angle of incidence with the pupil stop ranging from $\pm 40^\circ$ in 10° increments. From Fig. 1, it is apparent that there is a small tilt and displacement of the crystalline lens, which was required in order to satisfy the known asymmetries of the eye's aberrations [8,15,19,28,74].

For the data presented in this section, a negative eccentricity corresponded to the nasal retina along the horizontal meridian and the inferior retina along the vertical direction. Additionally, in order to make direct comparisons, the aberrations for all of the eye models were calculated using a 4 mm pupil aperture in the orientation of retina to cornea.

We used the RMS wavefront error to represent the overall optical accuracy of an eye model as compared with measured data. Figure 2 plots the RMS wavefront error as a function of retinal eccentricity for six modern eye models [8,41,46,47,50,74] and our proposed eye model along the horizontal meridian (see Fig. S2 in Supplement 1 for vertical meridian). For each eye model, the RMS wavefront error was calculated by subtracting each of the first 15 Zernike terms (excluding piston, tip, and tilt) from the average of the measured wavefront data [28], squaring the difference, averaging the squares, and then taking the square root of the average. The on-axis (0°) defocus magnitude was subtracted for each eye model because the existing eye models were designed with

different magnitudes of central refractive error. This subtraction process permitted a fairer comparison of the changes with eccentricity by vertically shifting the defocus curves of Figs. 2 and 3, and Figs. S2 and S3 in Supplement 1. Also, most imaging systems include the ability to compensate defocus on-axis, so the central refractive error is commonly eliminated. Please note that the kinks at -15° are due to the optic nerve obfuscating the measured wavefront data [28].

While Fig. 2 shows the overall performance of the various eye models, Fig. 3 shows their performance when separated into individual aberration terms for the horizontal meridian (see Fig. S3 in Supplement 1 for vertical meridian). The most significant aberration terms as determined by the measured data set were found to be oblique astigmatism [Fig. 3(a)], defocus [Fig. 3(b)], vertical astigmatism [Fig. 3(c)], coma [Fig. 3(d)], trefoil [Fig. 3(e)] and spherical aberration [Fig. 3(f)]. The most commonly used ophthalmic metrics, mean spherical refraction and cylinder, are shown in Figs. 3(g) and 3(h), respectively. The on-axis defocus aberration was removed for all eye models in order to compare best how each model varied with retinal eccentricity.

Figure 4 plots the 2D matrix of wavefront data for the 10 subjects against the proposed eye model. The wavefront data was decomposed into the dominant Zernike aberration terms. Data was acquired in 5° steps along the vertical and 1° steps along the horizontal for fields of view of 50° and 80° , respectively. The data was median-filtered along the horizontal direction in order to mitigate artifacts due to irregular wavefront measurements. Like the previous two figures, on-axis mean sphere was subtracted in order to emphasize how defocus varied with retinal eccentricity.

In order to demonstrate visually how our eye model represents the aberrations of the human eye, we compared the theoretical point spread functions of light focused onto the retina. Because focal spot sizes were not measured directly in the subject data, we chose to compare the spots predicted through an ideal lens transfer function. Wavefront profiles taken from the pupil of the measured and model eyes (Fig. S4 in Supplement 1) were propagated to the retina using the Fresnel kernel for a range of eccentricities along the horizontal meridian. It is important to note that the wavefront data used for the phase profiles in Fig. S4 in Supplement 1 were obtained using light that originated from point sources on the retina. The projected spot sizes at the retina were compared against two wide-field eye models, namely Navarro's wide-field [47] and Goncharov and Dainty's GRIN-based [50] schematic eyes (Fig. 5). The focal spot sizes predicted by this method should be representative of a double-pass imaging system, where light enters the eye at various angles of incidence.

The measured data used to constrain the eye model was acquired at a wavelength of 780 nm. In order to extend the applicability of our eye model to other wavelengths of interest, we incorporated known values of chromatic dispersion into the various optical media. Figure 6 plots the chromatic focal shift as a function of retinal eccentricity for the various models and the measured data set of [74]. The chromatic focal shift was calculated as the difference in mean sphere of the red (671 nm) and blue (475 nm) focal points. The calculation was performed

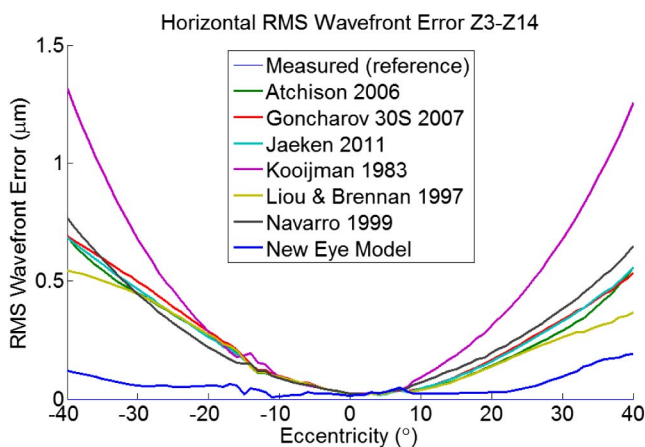


Fig. 2. RMS wavefront error of the various eye models as compared to the measured wavefront data set along the horizontal meridian. The on-axis (0°) defocus magnitude for each eye model was subtracted from the defocus value of the other eccentricities in order to illustrate more clearly the variation in RMS wavefront error with retinal eccentricity. The standard deviation of the measured data set was $\sim 0.138 \mu\text{m}$.

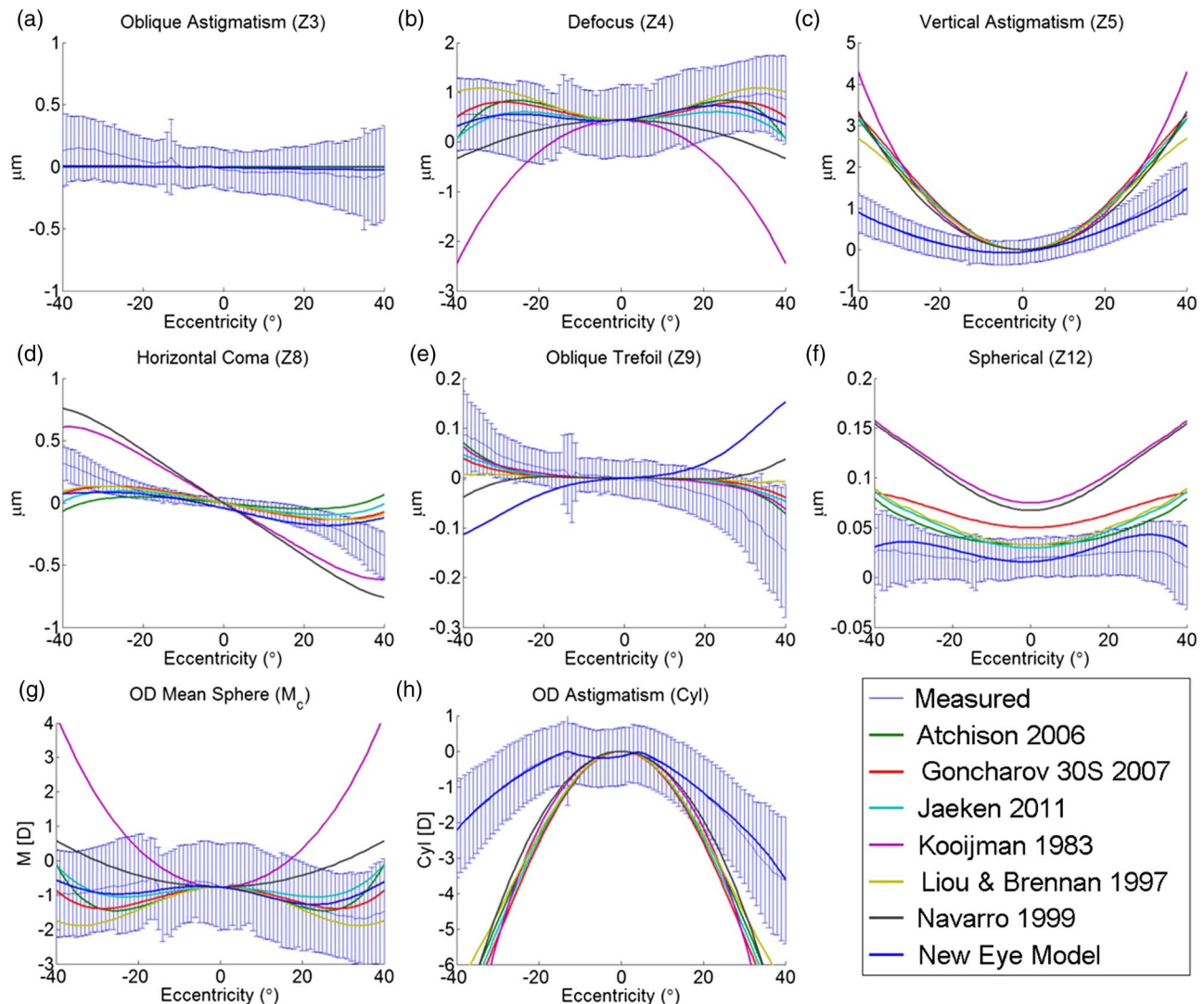


Fig. 3. Plots demonstrating individual Zernike aberration terms versus retinal eccentricity across the horizontal meridian. The most significant Zernike aberrations include (a) oblique astigmatism, (b) defocus, (c) vertical astigmatism, (d) horizontal coma, (e) oblique trefoil, and (f) spherical aberration. The key ophthalmic terms of (g) mean sphere and (h) cylinder are displayed as well. The error bars correspond to the standard deviation in the measured data set over the 101 tested eyes.

in object space, because the focal point metric was derived from the defocus wavefront aberration term. A GRIN dispersion profile taken from [74] was incorporated into the Liou and Brennan and the Goncharov 30S eye models. Adding dispersion to the crystalline lens was required in order to get realistic predictions of the on-axis LCA and off-axis chromatic focal shift.

4. DISCUSSION

Our schematic eye shows a significant improvement over the existing models in overall wavefront error. Figure 2 demonstrates how the collective aberrations of each eye model change with retinal eccentricity as compared to the horizontal meridian of the experimentally measured data. Most of the eye models have similar performance to the measured data within the first $\pm 5^\circ$ of the optical axis, but only the proposed model accurately represents both the on-axis and off-axis wavefront

aberrations. The previous models show declining reliability in the periphery, and this improvement is most notable at the extent of the periphery, where our model exhibits an improvement in RMS wavefront error of $0.1777 \mu\text{m}$ over the next best model. As the total RMS wavefront aberration in the measured data set at the extent of the periphery is roughly $0.18 \mu\text{m}$, our model offers a noteworthy improvement in optical accuracy to even the next best performing model.

The collective aberration performance along the vertical meridian (Fig. S2 in Supplement 1) also demonstrates our model's agreement with the measured data. Again, within 5° of the central axis most models perform similarly, but our model better represents the measured data in the periphery, with an improvement in RMS wavefront error of $0.1788 \mu\text{m}$.

While the overall performance of our eye model (Fig. 2 and Fig. S2 in Supplement 1) is better, even the individual aberration terms (Fig. 3 and Fig. S3 in Supplement 1) outperform the existing models in the retinal periphery. The other eye

models become unreliable largely due to an overestimation of astigmatism [Figs. 3(a), 3(c), and 3(h) and Figs. S3(a) and S3(c) in Supplement 1]. Additionally, because the other models use rotationally symmetric optics, they are unable to accommodate the asymmetric optical properties of actual eyes, which are observable clearly in the defocus [Fig. 3(b)], astigmatism [Figs. 3(a) and 3(c)], and coma [Fig. 3(d)] terms. Less asymmetry is observed in the vertical direction (Fig. S3 in Supplement 1), which is why the tilt and decentration have smaller magnitudes than those pertaining to the horizontal (Table 1). Shifting the location of the central axis of the retinal imaging plane of the other eye models would not improve their optical asymmetry, as the rates of change of the aberrations in the positive and negative directions are different. This trend is most apparent when visualizing the derivatives (not shown) of the astigmatism, coma, and trefoil terms. In summary, our model is able to incorporate both the asymmetry in optical performance as well as the overall aberration magnitudes as a function of eccentricity.

The magnitude of the aberrations is smaller on-axis, and typically, spherical aberration is the dominant term [Fig. 3(f)]. Defocus is the other major on-axis aberration, but often it is compensated externally in imaging systems with the use of corrective optics, such as Badal optometers. Therefore, it is important to note that our model shows a more accurate prediction of spherical aberration near the fovea, which is important when designing optical imaging systems aimed at resolving rods and cones [22,23,88].

The greatest shortcoming in our eye model is depicted in Fig. 3(e): an opposing trend in trefoil as compared to the measured data. While our model predicts the correct magnitude of trefoil on-axis, it quickly deviates from the intended trend in the periphery. However, since the trefoil term is an order of magnitude smaller than astigmatism, we do not believe that this observation is detrimental to the overall performance of the eye model. Tilting or decentering the lens cannot produce trefoil, but rather, trefoil depends on the intrinsic shape and structure of the cornea and crystalline lens. Upon investigation, this term was found to originate in the GRIN lens. Using a more sophisticated GRIN profile, which is discussed in Supplement 1, may allow us to maintain the overall aberration performance while correcting this minor inconsistency.

Figure 4 shows, for the 10 individuals with wavefronts measured at the 2D grid of points, that the newly proposed eye model is in excellent agreement with the measured data. The four largest Zernike aberrations are displayed, and the magnitudes and trends along all observable meridians appear to be well matched between the proposed eye model and measured data. Even though the optimization algorithm only constrained the wavefront aberrations along the horizontal and vertical meridians, the data throughout the extent of the field of view is reproduced correctly. Figure 4 confirms that the eye model can be useful across the full 2D field of view and that the proposed optimization method of Fig. S1 in Supplement 1 is capable of enforcing optical trends beyond those defined explicitly in the merit function.

The asymmetry of the eye may contribute to the paradoxical difference in optical and visual axes, which has been used to

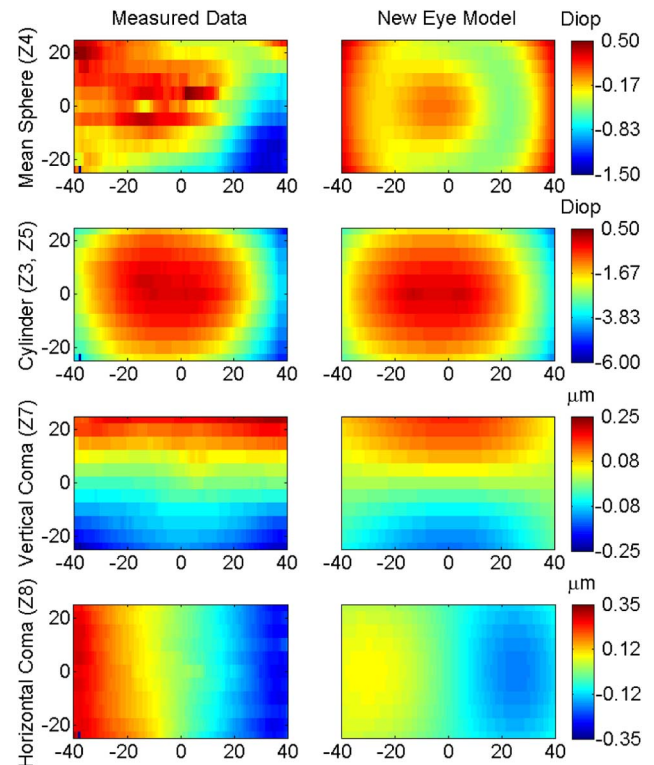


Fig. 4. Two-dimensional grid of measured wavefront data (left) compared with the aberrations calculated for the newly proposed eye model (right) in the pupil plane. Data was acquired in 1° steps along the horizontal and 5° steps along the vertical for 10 subjects. The aberration terms shown are the four largest contributors to the overall wavefront profile of the measured data set. On-axis defocus was subtracted from the mean sphere measurement in order to isolate the changes in defocus with retinal eccentricity.

explain the off-axis location of the fovea. From the literature, a $\sim 4^\circ$ difference in visual versus optical axis is reported. However, the average value has relatively little significance, as the individual variations in lens tilt are of the same magnitude. We observe this angle to be 2.99° along the horizontal and 0.62° along the vertical direction for our eye model. Since the asymmetry in aberrations is stronger along the horizontal than vertical meridian, it follows that the tilt would be smaller in this direction. Other works [16,47] have discussed the importance of the optical and visual axes, but they did not specifically modify their model to include the asymmetric features. We believe that our design is the first example of an eye model that provides a natural occurrence of this phenomenon by allowing the crystalline lens to be decentered and rotated during the optimization process. We provided no boundary constraints on the tilt and translation of the lens, and it found a set of values that fell within the anatomical observations of [81,82].

Figure 5 shows that our eye model more closely mirrors the theoretical focal spot profile on the retina as compared to the two other wide-field eye models. As expected in all eye models, we see an increase in spot size and therefore decrease in imaging performance with retinal eccentricity; however, both the shapes and sizes of the point spread functions predicted by our eye model more closely resemble the spots anticipated from the measured data. Being able to accurately predict the spot size

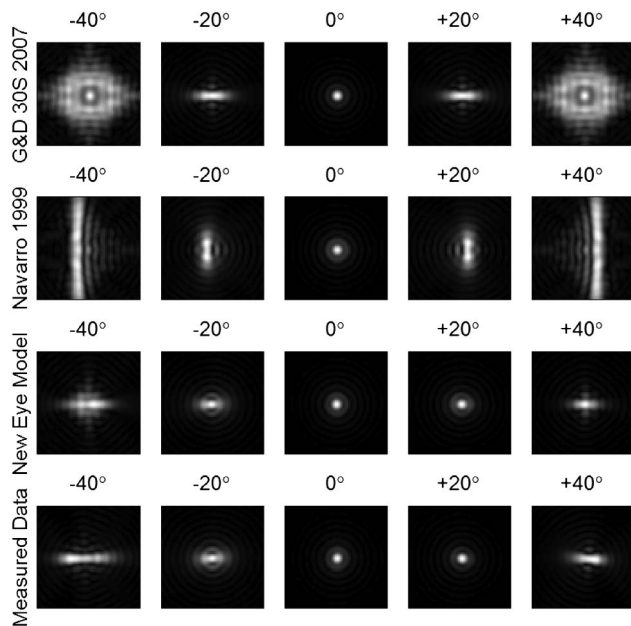


Fig. 5. Diagrams representing the theoretical focal spot profile of a perfectly collimated beam entering the eye at varying field angles along the horizontal meridian for two wide-field schematic eyes (Navarro [47] and G&D 30S [50]), our proposed eye, and the average of the measured data set [28].

and how images are blurred over the entire retina is important for both foveal and peripheral visual processing studies.

The images in Fig. 5 foreshadow the challenges of designing a system capable of imaging the proposed eye model and, by extension, real human eyes. By engineering optical elements that preemptively distort the light entering the eye, a system could both reduce the overall spot size at the retina and make the spot size more homogenous with the angle of illumination. This would be a crucial feature in the design of yet-to-be imagined wide-field imaging systems that require a high degree of spatial resolution throughout a large field of view.

We expect similar quantities of chromatic focal shift for the various eye models because, as discussed in [74], factors related to the increase of axial length and refractive index of the eye, including vitreous chamber size, GRIN of the crystalline lens, shape of the retina, and vignetting of the pupil, do not have significant influence over the chromatic focal shift. Figure 6 shows a similar trend of chromatic focal shift versus eccentricity for all of the tested eye models as well as the measured data set of [74]. The Jaeken 2011 (teal) curve in Fig. 6 was previously shown to be in close agreement with both myopic and emmetropic eyes [74]. Our eye model is in good agreement with this curve, but predicts a slightly flatter increase with eccentricity. Thibos *et al.* [44] estimate an on-axis LCA of ~ 1.06 D, and our eye model predicts a value of 1.057 D, which is within the standard deviation of the measurements. Also, our eye model incorporates the subtle asymmetric differences in chromatic focal shift observed in experimental measurements. Overall, we expect our eye model to be valid for a range of wavelengths, as it exhibits a dispersion profile that is comparable to the existing models.

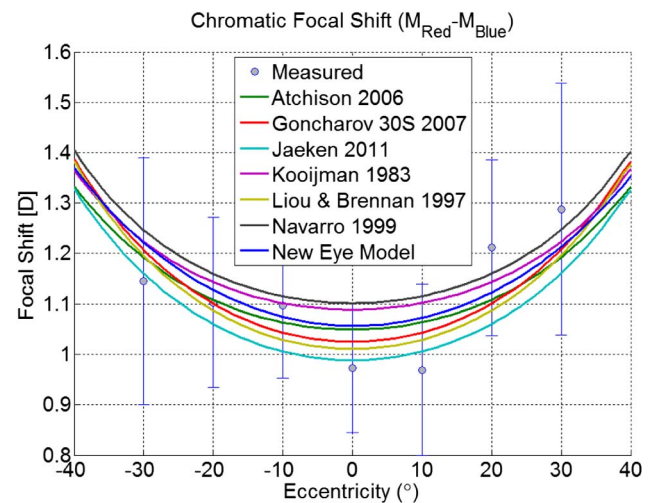


Fig. 6. Comparison of chromatic focal shift for various eye models as a function of retinal eccentricity. The chromatic focal shift was calculated as the difference in mean sphere of the red (671 nm) and blue (475 nm) focal points. The error bars of the measured data set correspond to the standard deviation between 11 individuals.

The figures throughout this work were calculated with the model oriented such that light originated at the retina and propagated to the cornea. This orientation was chosen because it models most accurately ophthalmic wavefronts measured by a Shack–Hartmann wavefront sensor. Though instrument designers may prefer that the model be oriented from cornea to retina in order to evaluate the spot size of existing and new designs, we recommend using our model in its presented orientation due to a limitation in GRIN lens representation in Zemax. We believe that this issue exists with previous GRIN-based eye models; further discussion is provided in Supplement 1.

The eye modeling optimization technique presented in this work could be further aided by corneal topography and tomography techniques [89–92]. Systems that are able to measure simultaneously the cornea and lens curvatures, namely extended-depth optical coherence tomography [93,94], are especially appealing for this application. For this work, the boundary limits in the optimization routine were referenced from the literature, but incorporating each individual's anatomical parameters would complement the existing wide-field aberration data by allowing a direct comparison of the model's fitted anatomical parameters to the mean of the measured population group.

One major criticism for generic eye models is that they only represent the average of a group of people and that specialized eye models, like the personalized models proposed in [5,48,49], can be useful in the design of imaging instruments. While we agree that specialized eye models may be helpful in that they can offer additional insight into a specific patient's ophthalmology, Fig. 7 shows that even when divided into central refractive groups, there are persisting trends in the dominant aberration terms except for defocus. Instrumentation cannot be designed to accommodate the needs of every individual without the use of adaptive optics, but removing the bulk of the aberrations by mitigating the effect of the

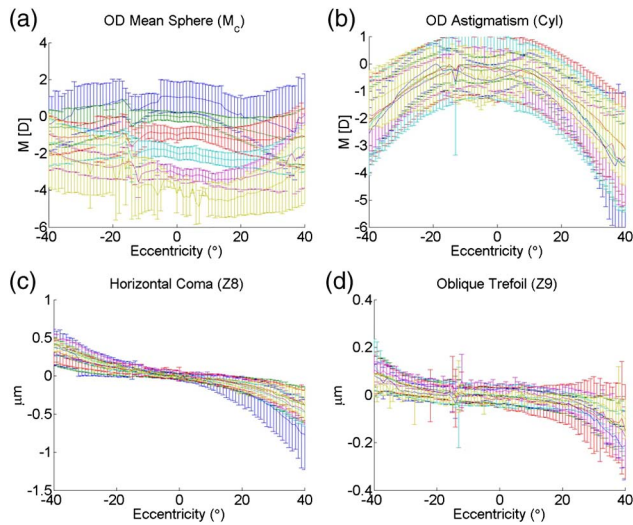


Fig. 7. Plots showing the variation of Zernike coefficients across the horizontal meridian for eyes (101 total) divided into subgroups based upon central refractive error. The colors represent different magnitudes of central refractive error within 1 D ranges. (a) Mean sphere, (b) cylinder, (c) coma, and (d) trefoil are shown because they are the largest varying aberrations in the measured data set along the horizontal meridian. Error bars correspond to the standard deviation within a given refractive group.

generalized trends has the potential to greatly improve imaging resolution. Additionally, as suggested in [28], foveal refractive errors tend to be correlated with peripheral defocus, so devising an interchangeable lens based on central refractive error could help to mitigate the parasitic effects due to the large interpatient variability found in the peripheral retina. Therefore, we posit that optical instrumentation that is designed to counterbalance the eye's aberration trends, simultaneously improving the resolution and simplifying the design of wide-field imaging systems, should be possible using the proposed model.

Additionally, as more aberration data becomes available, eye models can be designed for specific subgroups, including central refraction, gender, ethnicity, and age. Even patient-specific models, like those first proposed by [48], could be created using the reverse building eye modeling technique outlined in Fig. S1 in Supplement 1. These topics, among many more, are areas of advancement that have yet to be explored fully.

5. CONCLUSION

We have developed an asymmetric, anatomically inspired, and optically accurate wide-field schematic eye based on measured wavefront data. To our knowledge, this is the first eye model that portrays accurately the optical performance, including both low-order and high-order Zernike terms, across a wide field of view within anatomical constraints. We compared our proposed eye model to previously published models as well as experimentally measured Shack–Hartmann wavefront data. Our model shows better agreement with the measured data along all meridians, both comprehensively and for almost the entire set of Zernike terms at all field angles. Our model especially excels at predicting the aberrations of the retinal periphery. All of the eye models studied have a similar

dispersion profile as validated by measurements of chromatic focal shift as a function of eccentricity. The proposed eye model has the potential to impact both the design of wide-field imaging instruments as well as the study of the peripheral optics of the human eye.

Second, we have outlined a robust reverse building eye modeling technique that is capable of predicting trends beyond those defined explicitly in the optimization routine. Though we constrained our model's aberration profile from -40° to $+40^\circ$ in 10° steps (horizontal) and -20° to $+20^\circ$ in 10° steps (vertical), our model was able to reproduce the measured data trends smoothly throughout the entire range of eccentricities presented in a 2D grid of wavefront measurements. Also, our model predicted accurately a number of commonly accepted optical properties, including lens power, total power, longitudinal spherical aberration, spherical aberration at a different pupil diameter, and eye length, and it was able to evoke an anatomically plausible, yet unsolicited, tilt and decentration of the crystalline lens. Translocation of the lens was explored previously by Atchison in 2006 [8], but we believe that we are the first to allow the lens to tilt and translate as a natural product of the optimization process.

FUNDING INFORMATION

European Research Council (ERC) (ERC-2013-AdG-339228); National Science Foundation (NSF) (CBET-1-03905); SEIDI, Spain (FIS2013-41237-R).

ACKNOWLEDGMENT

We appreciate the many thoughtful discussions and contributions to the writing of this paper from Dr. Anthony Kuo. We would also like to acknowledge Lucia Hervella for gathering and processing the 2D data set. James Polans was supported by a National Science Foundation Graduate Research Fellowship.

See Supplement 1 for supporting content.

REFERENCES

1. P. Artal and J. Tabernero, "The eye's aplanatic answer," *Nat. Photonics* **2**, 586–589 (2008).
2. P. Artal, "Optics of the eye and its impact in vision: a tutorial," *Adv. Opt. Photon.* **6**, 340–367 (2014).
3. P. G. Gobbi, F. Carones, and R. Brancato, "Optical eye model for photo-refractive surgery evaluation," *Proc. SPIE* **3591**, 10–21 (1999).
4. E. O. Curatu, G. H. Pettit, and J. A. Campin, "Customized schematic eye model for refraction correction design based on ocular wavefront and corneal topography measurements," *Proc. SPIE* **4611**, 165–175 (2002).
5. J. Tabernero, P. Piers, A. Benito, M. Redondo, and P. Artal, "Predicting the optical performance of eyes implanted with IOLs to correct spherical aberration," *Invest. Ophthalmol. Vis. Sci.* **47**, 4651–4658 (2006).
6. S. Norrby, P. Piers, C. Campbell, and M. D. van der Mooren, "Model eyes for evaluation of intraocular lenses," *Appl. Opt.* **46**, 6595–6605 (2007).
7. D. A. Atchison, E. L. Markwell, S. Kasthurirangan, J. M. Pope, G. Smith, and P. G. Swann, "Age-related changes in optical and biometric characteristics of emmetropic eyes," *J. Vis.* **8**(4):29, 1–20 (2008).

8. D. A. Atchison, "Optical models for human myopic eyes," *Vis. Res.* **46**, 2236–2250 (2006).
9. J. W. Blaker, "A comprehensive model of the aging, accommodative adult eye," in *Technical Digest on Ophthalmic and Visual Optics*, (Optical Society of America, 1991), Vol. **2**, pp. 28–31.
10. K. Zadnik, R. E. Manny, J. A. Yu, G. L. Mitchell, S. A. Cotter, J. C. Quirralte, M. D. Shipp, N. E. Friedman, R. N. Kleinstein, T. W. Walker, L. A. Jones, M. L. Moeschberger, D. O. Mutti, and C. L. Evaluti, "Ocular component data in schoolchildren as a function of age and gender," *Optom. Vis. Sci.* **80**, 226–236 (2003).
11. D. A. Atchison, N. Pritchard, S. D. White, and A. M. Griffiths, "Influence of age on peripheral refraction," *Vis. Res.* **45**, 715–720 (2005).
12. J. S. McLellan, S. Marcos, and S. A. Burns, "Age-related changes in monochromatic wave aberrations of the human eye," *Invest. Ophthalmol. Vis. Sci.* **42**, 1390–1395 (2001).
13. K. Ninn-Pedersen, "Relationships between preoperative astigmatism and corneal optical power, axial length, intraocular pressure, gender, and patient age," *J. Refract. Surg.* **12**, 472–482 (1996).
14. R. Navarro, J. Santamaria, and J. Bescos, "Accommodation-dependent model of the human-eye with aspherics," *J. Opt. Soc. Am. A* **2**, 1273–1281 (1985).
15. L. Lundstrom, A. Mira-Agudelo, and P. Artal, "Peripheral optical errors and their change with accommodation differ between emmetropic and myopic eyes," *J. Vis.* **9**(6):17, 1–11 (2009).
16. M. M. Kong, Z. S. Gao, X. H. Li, S. H. Ding, X. M. Qu, and M. Q. Yu, "A generic eye model by reverse building based on Chinese population," *Opt. Express* **17**, 13283–13297 (2009).
17. J. C. He, S. A. Burns, and S. Marcos, "Monochromatic aberrations in the accommodated human eye," *Vis. Res.* **40**, 41–48 (2000).
18. A. Popielek-Masajada and H. Kasprzak, "Model of the optical system of the human eye during accommodation," *Ophthalm. Phys. Opt.* **22**, 201–208 (2002).
19. D. A. Atchison, N. Pritchard, and K. L. Schmid, "Peripheral refraction along the horizontal and vertical visual fields in myopia," *Vis. Res.* **46**, 1450–1458 (2006).
20. J. Hoogerheide, F. Rempt, and W. G. H. Hoogenboom, "Acquired myopia in young pilots," *Ophthalmologica* **163**, 209–215 (1971).
21. E. L. Smith, C. S. Kee, R. Ramamirtham, Y. Qiao-Grider, and L. F. Hung, "Peripheral vision can influence eye growth and refractive development in infant monkeys," *Invest. Ophthalmol. Vis. Sci.* **46**, 3965–3972 (2005).
22. F. LaRocca, A. H. Dhalla, M. P. Kelly, S. Farsiu, and J. A. Izatt, "Optimization of confocal scanning laser ophthalmoscope design," *J. Biomed. Opt.* **18**, 076015 (2013).
23. F. LaRocca, D. Nankivil, S. Farsiu, and J. A. Izatt, "Handheld simultaneous scanning laser ophthalmoscopy and optical coherence tomography system," *Biomed. Opt. Express* **4**, 2307–2321 (2013).
24. D. R. Williams, P. Artal, R. Navarro, M. J. McMahon, and D. H. Brainard, "Off-axis optical quality and retinal sampling in the human eye," *Vis. Res.* **36**, 1103–1114 (1996).
25. R. Navarro, E. Moreno, and C. Dorronsoro, "Monochromatic aberrations and point-spread functions of the human eye across the visual field," *J. Opt. Soc. Am. A* **15**, 2522–2529 (1998).
26. A. Guirao and P. Artal, "Off-axis monochromatic aberrations estimated from double pass measurements in the human eye," *Vis. Res.* **39**, 207–217 (1999).
27. D. A. Atchison and D. H. Scott, "Monochromatic aberrations of human eyes in the horizontal visual field," *J. Opt. Soc. Am. A* **19**, 2180–2184 (2002).
28. B. Jaeken and P. Artal, "Optical quality of emmetropic and myopic eyes in the periphery measured with high-angular resolution," *Investig. Ophthalmol. Vis. Sci.* **53**, 3405–3413 (2012).
29. E. A. Swanson, J. A. Izatt, M. R. Hee, D. Huang, C. P. Lin, J. S. Schuman, C. A. Puliafito, and J. G. Fujimoto, "In-vivo retinal imaging by optical coherence tomography," *Opt. Lett.* **18**, 1864–1866 (1993).
30. D. Huang, E. A. Swanson, C. P. Lin, J. S. Schuman, W. G. Stinson, W. Chang, M. R. Hee, T. Flotte, K. Gregory, C. A. Puliafito, and J. G. Fujimoto, "Optical coherence tomography," *Science* **254**, 1178–1181 (1991).
31. J. J. Hunter, B. Masella, A. Dubra, R. Sharma, L. Yin, W. H. Merigan, G. Palczewska, K. Palczewski, and D. R. Williams, "Images of photoreceptors in living primate eyes using adaptive optics two-photon ophthalmoscopy," *Biomed. Opt. Express* **2**, 139–148 (2011).
32. G. Palczewska, T. Maeda, Y. Imanishi, W. Y. Sun, Y. Chen, D. R. Williams, D. W. Piston, A. Maeda, and K. Palczewski, "Noninvasive multiphoton fluorescence microscopy resolves retinol and retinal condensation products in mouse eyes," *Nat. Med.* **16**, 1444–1449 (2010).
33. M. M. Wessel, G. D. Aaker, G. Parlitsis, M. Cho, D. J. D'Amico, and S. Kiss, "Ultra-wide-field angiography improves the detection and classification of diabetic retinopathy," *Retina* **32**, 785–791 (2012).
34. A. Manivannan, J. Plskova, A. Farrow, S. McKay, P. F. Sharp, and J. V. Forrester, "Ultra-wide-field fluorescein angiography of the ocular fundus," *Am. J. Ophthalmol.* **140**, 525–527 (2005).
35. S. Nakao, R. Arita, T. Nakama, H. Yoshikawa, S. Yoshida, H. Enaida, A. Hafezi-Moghadam, T. Matsui, and T. Ishibashi, "Wide-field laser ophthalmoscopy for mice: a novel evaluation system for retinal/choroidal angiogenesis in mice," *Investig. Ophthalmol. Vis. Sci.* **54**, 5288–5293 (2013).
36. P. Artal and J. Tabernero, "Optics of human eye: 400 years of exploration from Galileo's time," *Appl. Opt.* **49**, D123–D130 (2010).
37. A. Gullstrand, *von Helmholtz Handbuch der Physiologischen Optik*, 3rd ed., Appendix II and IV (Voss, 1909), Vol. **1**, pp. 382–415.
38. Y. Le Grand, *Optique Physiologique I* (Editions de la Revue d'Optique, 1953), Vol. **52**.
39. H. Emsley, *Visual Optics* (Butterworth, 1962), Vol. **40–42**, pp. 460–461.
40. W. Lotmar, "Theoretical eye model with aspherics," *J. Opt. Soc. Am.* **61**, 1522–1529 (1971).
41. A. C. Kooijman, "Light-distribution on the retina of a wide-angle theoretical eye," *J. Opt. Soc. Am.* **73**, 1544–1550 (1983).
42. O. Pomerantzef, M. Pankratov, G. J. Wang, and P. Dufault, "Wide-angle optical-model of the eye," *Am. J. Optom. Physiol. Opt.* **61**, 166–176 (1984).
43. J. W. Blaker, "Toward an adaptive model of the human-eye," *J. Opt. Soc. Am.* **70**, 220–223 (1980).
44. L. N. Thibos, M. Ye, X. X. Zhang, and A. Bradley, "The chromatic eye: a new reduced-eye model of ocular chromatic aberration in humans," *Appl. Opt.* **31**, 3594–3600 (1992).
45. M. Ye, X. X. Zhang, L. Thibos, and A. Bradley, "A new single-surface model eye that accurately predicts chromatic and spherical aberrations of the human eye," *Investig. Ophthalmol. Vis. Sci.* **34**, 774–777 (1993).
46. H. L. Liou and N. A. Brennan, "Anatomically accurate, finite model eye for optical modeling," *J. Opt. Soc. Am. A* **14**, 1684–1695 (1997).
47. I. Escudero-Sanz and R. Navarro, "Off-axis aberrations of a wide-angle schematic eye model," *J. Opt. Soc. Am. A* **16**, 1881–1891 (1999).
48. R. Navarro, L. Gonzalez, and J. L. Hernandez-Matamoros, "On the prediction of optical aberrations by personalized eye models," *Optom. Vis. Sci.* **83**, 371–381 (2006).
49. P. Rosales and S. Marcos, "Customized computer models of eyes with intraocular lenses," *Opt. Express* **15**, 2204–2218 (2007).
50. A. V. Goncharov and C. Dainty, "Wide-field schematic eye models with gradient-index lens," *J. Opt. Soc. Am. A* **24**, 2157–2174 (2007).
51. L. N. Thibos, M. Ye, X. X. Zhang, and A. Bradley, "Spherical aberration of the reduced schematic eye with elliptical refracting surface," *Optom. Vis. Sci.* **74**, 548–556 (1997).
52. J. A. Diaz, C. Pizarro, and J. Arasa, "Single dispersive gradient-index profile for the aging human lens," *J. Opt. Soc. Am. A* **25**, 250–261 (2008).
53. G. Smith, P. Bedggood, R. Ashman, M. Daaboul, and A. Metha, "Exploring ocular aberrations with a schematic human eye model," *Optom. Vis. Sci.* **85**, 330–340 (2008).
54. C. E. Campbell, "Nested shell optical model of the lens of the human eye," *J. Opt. Soc. Am. A* **27**, 2432–2441 (2010).

55. Y. L. Chen, L. Shi, J. W. L. Lewis, and M. Wang, "Normal and diseased personal eye modeling using age-appropriate lens parameters," *Opt. Express* **20**, 12498–12507 (2012).
56. J. Santamaria, P. Artal, and J. Bescos, "Determination of the point-spread function of human eyes using a hybrid optical-digital method," *J. Opt. Soc. Am. A* **4**, 1109–1114 (1987).
57. R. Navarro and M. A. Losada, "Aberrations and relative efficiency of light pencils in the living human eye," *Optom. Vis. Sci.* **74**, 540–547 (1997).
58. W. Lotmar and T. Lotmar, "Peripheral astigmatism in human eye: experimental-data and theoretical model predictions," *J. Opt. Soc. Am.* **64**, 510–513 (1974).
59. R. Navarro, P. Artal, and D. R. Williams, "Modulation transfer of the human eye as a function of retinal eccentricity," *J. Opt. Soc. Am. A* **10**, 201–212 (1993).
60. J. Gustafsson, E. Terenius, J. Buchheister, and P. Unsbo, "Peripheral astigmatism in emmetropic eyes," *Ophthal. Physiol. Opt.* **21**, 393–400 (2001).
61. D. A. Atchison, D. H. Scott, and W. N. Charman, "Hartmann–Shack technique and refraction across the horizontal visual field," *J. Opt. Soc. Am. A* **20**, 965–973 (2003).
62. L. Lundstrom, P. Unsbo, and J. Gustafsson, "Off-axis wave front measurements for optical correction in eccentric viewing," *J. Biomed. Opt.* **10**, 034002 (2005).
63. Y. Benny, S. Manzanera, P. M. Prieto, E. N. Ribak, and P. Artal, "Wide-angle chromatic aberration corrector for the human eye," *J. Opt. Soc. Am. A* **24**, 1538–1544 (2007).
64. C. Fedtke, K. Ehrmann, and B. A. Holden, "A review of peripheral refraction techniques," *Optom. Vis. Sci.* **86**, 429–446 (2009).
65. X. Wei and L. Thibos, "Design and validation of a scanning Shack Hartmann aberrometer for measurements of the eye over a wide field of view," *Opt. Express* **18**, 1134–1143 (2010).
66. J. Z. Liang, B. Grimm, S. Goelz, and J. F. Bille, "Objective measurement of wave aberrations of the human eye with the use of a Hartmann–Shack wave-front sensor," *J. Opt. Soc. Am. A* **11**, 1949–1957 (1994).
67. P. M. Prieto, F. Vargas-Martin, S. Goelz, and P. Artal, "Analysis of the performance of the Hartmann–Shack sensor in the human eye," *J. Opt. Soc. Am. A* **17**, 1388–1398 (2000).
68. J. Z. Liang and D. R. Williams, "Aberrations and retinal image quality of the normal human eye," *J. Opt. Soc. Am. A* **14**, 2873–2883 (1997).
69. B. Jaeken, L. Lundstrom, and P. Artal, "Fast scanning peripheral wave-front sensor for the human eye," *Opt. Express* **19**, 7903–7913 (2011).
70. R. C. Bakaraju, K. Ehrmann, E. Papas, and A. Ho, "Finite schematic eye models and their accuracy to in-vivo data," *Vis. Res.* **48**, 1681–1694 (2008).
71. X. Wei and L. Thibos, "Modeling the eye's optical system by ocular wavefront tomography," *Opt. Express* **16**, 20490–20502 (2008).
72. L. Lundstrom, J. Gustafsson, and P. Unsbo, "Population distribution of wavefront aberrations in the peripheral human eye," *J. Opt. Soc. Am. A* **26**, 2192–2198 (2009).
73. D. A. Atchison and G. Smith, "Chromatic dispersions of the ocular media of human eyes," *J. Opt. Soc. Am. A* **22**, 29–37 (2005).
74. B. Jaeken, L. Lundstrom, and P. Artal, "Peripheral aberrations in the human eye for different wavelengths: off-axis chromatic aberration," *J. Opt. Soc. Am. A* **28**, 1871–1879 (2011).
75. J. J. Rozema, D. A. Atchison, and M. J. Tassignon, "Statistical eye model for normal eyes," *Investig. Ophthalmol. Vis. Sci.* **52**, 4525–4533 (2011).
76. J. A. Sakamoto, H. H. Barrett, and A. V. Goncharov, "Inverse optical design of the human eye using likelihood methods and wavefront sensing," *Opt. Express* **16**, 304–314 (2008).
77. A. V. Goncharov, M. Nowakowski, M. T. Sheehan, and C. Dainty, "Reconstruction of the optical system of the human eye with reverse ray-tracing," *Opt. Express* **16**, 1692–1703 (2008).
78. N. Asano-Kato, I. Toda, C. Sakai, Y. Hori-Komai, Y. Takano, M. Dogru, and K. Tsubota, "Pupil decentration and iris tilting detected by Orbscan: anatomic variations among healthy subjects and influence on outcomes of laser refractive surgeries," *J. Cataract Refract. Surg.* **31**, 1938–1942 (2005).
79. D. A. Atchison, C. E. Jones, K. L. Schmid, N. Pritchard, J. M. Pope, W. E. Strugnell, and R. A. Riley, "Eye shape in emmetropia and myopia," *Investig. Ophthalmol. Vis. Sci.* **45**, 3380–3386 (2004).
80. D. A. Atchison, N. Pritchard, K. L. Schmid, D. H. Scott, C. E. Jones, and J. M. Pope, "Shape of the retinal surface in emmetropia and myopia," *Invest. Ophthalmol. Vis. Sci.* **46**, 2698–2707 (2005).
81. Y. Chang, H. M. Wu, and Y. F. Lin, "The axial misalignment between ocular lens and cornea observed by MRI (I): at fixed accommodative state," *Vis. Res.* **47**, 71–84 (2007).
82. F. Schaeffel, "Binocular lens tilt and decentration measurements in healthy subjects with phakic eyes," *Investig. Ophthalmol. Vis. Sci.* **49**, 2216–2222 (2008).
83. P. Rosales and S. Marcos, "Phakometry and lens tilt and decentration using a custom-developed Purkinje imaging apparatus: validation and measurements," *J. Opt. Soc. Am. A* **23**, 509–520 (2006).
84. J. Tabernero, A. Benito, V. Nourrit, and P. Artal, "Instrument for measuring the misalignments of ocular surfaces," *Opt. Express* **14**, 10945–10956 (2006).
85. C. E. Jones, D. A. Atchison, R. Meder, and J. M. Pope, "Refractive index distribution and optical properties of the isolated human lens measured using magnetic resonance imaging (MRI)," *Vis. Res.* **45**, 2352–2366 (2005).
86. L. N. Thibos, X. Hong, A. Bradley, and X. Cheng, "Statistical variation of aberration structure and image quality in a normal population of healthy eyes," *J. Opt. Soc. Am. A* **19**, 2329–2348 (2002).
87. J. Porter, A. Guirao, I. G. Cox, and D. R. Williams, "Monochromatic aberrations of the human eye in a large population," *J. Opt. Soc. Am. A* **18**, 1793–1803 (2001).
88. A. Roorda, F. Romero-Borja, W. J. Donnelly, H. Queener, T. J. Hebert, and M. C. W. Campbell, "Adaptive optics scanning laser ophthalmoscopy," *Opt. Express* **10**, 405–412 (2002).
89. R. P. McNabb, A. N. Kuo, and J. A. Izatt, "Quantitative single and multi-surface clinical corneal topography utilizing optical coherence tomography," *Opt. Lett.* **38**, 1212–1214 (2013).
90. F. LaRocca, S. J. Chiu, R. P. McNabb, A. N. Kuo, J. A. Izatt, and S. Farsiu, "Robust automatic segmentation of corneal layer boundaries in SDOCT images using graph theory and dynamic programming," *Biomed. Opt. Express* **2**, 1524–1538 (2011).
91. S. Ortiz, D. Siedlecki, P. Perez-Merino, N. Chia, A. de Castro, M. Szkulmowski, M. Wojtkowski, and S. Marcos, "Corneal topography from spectral optical coherence tomography (sOCT)," *Biomed. Opt. Express* **2**, 3232–3247 (2011).
92. S. Ortiz, D. Siedlecki, L. Remon, and S. Marcos, "Optical coherence tomography for quantitative surface topography," *Appl. Opt.* **48**, 6708–6715 (2009).
93. S. Ortiz, P. Perez-Merino, E. Gamba, A. de Castro, and S. Marcos, "In vivo human crystalline lens topography," *Biomed. Opt. Express* **3**, 2471–2488 (2012).
94. A. H. Dhalla, D. Nankivil, T. Bustamante, A. Kuo, and J. A. Izatt, "Simultaneous swept source optical coherence tomography of the anterior segment and retina using coherence revival," *Opt. Lett.* **37**, 1883–1885 (2012).